

Photonics of topological magnetic textures

Vakhtang Jandieri^{1,2}, Ramaz Khomeriki³, Daniel Erni²,
 Nicolas Tsagareli⁴, Qian Li⁵, Douglas H. Werner⁶, and Jamal Berakdar^{1*}

¹ Institut für Physik, Martin-Luther Universität, Halle-Wittenberg, D-06099 Halle, Germany

² General and Theoretical Electrical Engineering (ATE), Faculty of Engineering, University of Duisburg-Essen, and Center for Nanointegration Duisburg-Essen (CENIDE), D-47048 Duisburg, Germany

³ Physics Department, Tbilisi State University, 3 Chavchavadze, 0128 Tbilisi, Georgia

⁴ Department of Electrical and Computer Engineering, Binghamton

University, State University of New York, Binghamton, NY 13902, USA

⁵ State Key Laboratory of New Ceramics and Fine Processing, School of
 Materials Science and Engineering, Tsinghua University, Beijing 100084, China

⁶ Department of Electrical Engineering, The Pennsylvania State University, University Park, PA 16802, USA

*Corresponding author: Jamal.Berakdar@Physik.Uni-Halle.de

Topological textures in magnetically ordered materials are important case studies for fundamental research with promising applications in data science. They can also serve as photonic elements to mold electromagnetic fields endowing them with features inherent to the spin order, as demonstrated analytically and numerically in this work. A self-consistent theory is developed for the interaction of spatially structured electromagnetic fields with non-collinear, topologically non-trivial spin textures. A tractable numerical method is designed and implemented for the calculation of the formed magnetic/photonic textures in the entire simulation space. Numerical illustrations are presented for scattering from point-like singularities, i.e. Bloch points, in the magnetization vector fields, evidencing that the geometry and topology of the magnetic order results in photonic fields that embody orbital angular momentum, chirality as well as magnetoelectric densities. Features of the scattered fields can serve as a fingerprint for the underlying magnetic texture and its dynamics. The findings point to the potential of topological magnetic textures as a route to molding photonic fields.

I. INTRODUCTION

Emergence and characteristics of stable topological textures and quasiparticles such as vortices, skyrmions or hopfions (Hopf solitons) are well studied and documented in the context of field theories, for example in [1–11]. With experimental realizations of these textures in static magnetic and ferroelectric materials as well as in electromagnetic waves [12–20], much research has been devoted to their possible utilization in information storage, communication, and processing [21]. In this respect, means are necessary to controllably exploit, identify, and manipulate their geometric-topological features. The focus of this work is on the magneto-optical response as well as on the scattering, and formation of spatially structured electromagnetic fields due to non-collinear topological textures formed in a magnetization vector field. In particular, we present explicit results and simulations for point-like magnetic singularities with vanishing magnetic moments [22, 23]. This so-called Bloch-point (BP) singularity can be viewed as a magnetic monopole and can be surrounded by a hedgehog-type structure or other types of non-collinearities [22–27]; some examples are detailed below. On the microscopic level the formation of BP is dominated by the exchange interaction and hence the magnetic response should be much faster than the typical GHz magnonic response in homogeneous magnets. BPs have been studied in a wide range of materials and on different length scales, notably BPs in domains of

multilayers and skyrmion lattices or as engineered materials with structuring [24–37]. BP singularities are of relevance also for fundamental science, for instance as emulators of electron motion in a magnetic monopole field [38]. For applied science, their distinctive topological [39] nanometer scale, as well as energy scale [40] features make them a compelling option for data storage and processing [24–37]. To characterize and drive controllably Bloch points is however a challenge, mainly due to their vanishing magnetization. Clearly, footprints of their topological characteristics are left in their surrounding long-range magnetic order. Hence, a probe which couples directly to their intrinsic non-collinear structure would be highly desirable. Also the question of a possible use of BPs or similar textures as functional photonic elements needs to be clarified.

In this work we study the scattering and formation of structured electromagnetic (EM) waves from BPs, and illustrate the polarization distribution and the spatial structure of the fields, as reflected for example by the chirality density and/or the orbital angular momentum density. While propagating EM waves are bound in their spatial resolution to the diffraction limit, there is no such limit on the polarization texturing [41–47]. In fact, the EM fields used here can also be singular beams with the singularity occurring on the optical axis. In this way a spatial resolution on the nanometer scale of the magnetic singularity can be achieved. In recent years clear experimental and theoretical evidence has been accumulated on how to use singular

of spatially structured fields to access new information on matter [48–60], but so far a closed theory describing light-matter action-back-action, particularity in the context of magnetically ordered systems remains elusive. Such a theory would bridge the gap between topological photonics [61] and magneto photonics [62] to topological magnetic textures.

An important issue to clarify is how the singular magnetic texture responds to external EM fields and how the fields are modified by the magnetic texture, when the frequencies of these EM fields are in the range of magnetic excitations. Therefore, we will set up a coupled, self-consistent magnetic-photonic modeling scheme for the case involving a large photon number (classical EM fields) and where the length (energy) scales of relevance are much larger (smaller) than the atomistic ones. Under these conditions it is reasonable to work within classical field theories and incorporate the atomistic electronic information, as is customary with dielectric/permeability tensors.

To be explicit we focus here on BPs as a paradigm for highly non-collinear systems. Our theoretical formulation is however applicable to other types of nonlinearities such as vortices [63, 64], skyrmions, spin ice [65, 66], gyroids [67], or external magnetic fields imparted by other structured waves [68–71]. The specific system is manifested in the appropriate magnetic free energy density and the corresponding boundary conditions. Generally, the magnetic free energy density contains both the external magnetic field $\mathbf{H}_{\text{ext}}(\mathbf{r}, t)$ of the incoming EM waves and contributions from intrinsic magnetic interactions $\mathbf{H}(\mathbf{r}, t)$ such as exchange coupling. The dynamics of the local magnetization $\mathbf{M}(\mathbf{r}, t)$, described by the Landau-Lifshits-Gilbert equation implicitly updates for the magnetic field at time t' and space \mathbf{r}' to be used as an input value for Maxwell's equations to infer the electric flux density $\mathbf{D}(\mathbf{r}', t')$. The successive applications of this procedure accounts for multiple magnetic/electromagnetic scattering events. In the linear response regime, we analytically derive the frequency and wave-vector-dependent permeability tensor that can be used for the low-energy dynamics of the magnetic textures. A time-harmonic dependence of $e^{j\omega t}$ is assumed and omitted throughout the manuscript.

II. FORMAL CONSIDERATIONS

For non-collinear magnets, we seek a self-consistent spherical rigorous-coupled wave analysis for EM wave scattering in three-dimensions (3D). For instance, the theory should account for the inhomogeneities and dynamical response of the magnetic order spherically surrounding the BP (see the inset in Fig. 1). In the linear response regime, we wish to analytically obtain a magnetic permeability matrix and uncover the variation of its components along the radial direction and along the

polar angle. Hereby, we assume azimuthally homogeneous BPs. This is accomplished below where, technically, the method reduces the problem to the solution of a set of first-order coupled differential equations. Moreover, the field representations are then found using the eigenvectors and eigenvalues of the matrix generated by the Fourier components of the constant coefficients of the differential equations. Numerically, the approach uses the recursive algorithm based on matrix multiplication, which allows us to calculate the scattering characteristics for the BP efficiently. The method can deal numerically with various types of impinging electromagnetic waves and BPs such as hedgehog and twisted. For brevity only selected results are presented showing that the distinct magnetic order around the BP leads to an involved structure of the formed EM fields and the generation of optical chirality density and orbital angular momentum in a close vicinity to the BP. Also, we find a dominant azimuthal component of the Poynting vector close to the surface of the BP. Only the components of the reflected electric and magnetic fields that appear solely by an interaction of the incident waves with the BP show a sensitive behavior while transforming from the hedgehog to the twisted model.

The formulation below is developed for a magnetic insulator, meaning that no free currents/charges are present, and assumes that the dielectric response (and hence the relative dielectric permittivity ϵ_r) is nearly constant and homogeneous in the frequency regime of interest here. These restrictions are not fundamental but allow the magnetic/photonic effects to be singled out. The coupled field equations of motion for magneto-static/electromagnetic dynamics are given by

$$\begin{aligned} \frac{\partial \mathbf{M}(\mathbf{r}, t)}{\partial t} &= -g\mu_0 [\mathbf{M}(\mathbf{r}, t) \times \mathbf{H}_{\text{eff}}(\mathbf{r}, t)], \\ \nabla \times [\mathbf{H}(\mathbf{r}, t) + \mathbf{H}_{\text{ext}}(\mathbf{r}, t)] &= \epsilon_0 \epsilon_r \frac{\partial \mathbf{E}(\mathbf{r}, t)}{\partial t}, \\ \nabla \times \mathbf{E}(\mathbf{r}, t) &= -\mu_0 \frac{\partial}{\partial t} [\mathbf{H}(\mathbf{r}, t) + \mathbf{H}_{\text{ext}}(\mathbf{r}, t) + \mathbf{M}(\mathbf{r}, t)] \end{aligned} \quad (1)$$

where g is the gyromagnetic ratio, \mathbf{H} and \mathbf{H}_{ext} are the demagnetization and external magnetic fields, respectively, \mathbf{M} is the magnetization vector field, ϵ_0 and μ_0 are dielectric permittivity and magnetic permeability of free space. The electric polarization induced by BP spin-noncollinearities (e.g., as in [72]) is negligible. The external magnetic field \mathbf{H}_{ext} is related to the incident field and is defined by the boundary condition on a surface of the sphere enclosing the magnetic singularity (see the inset of Fig. 1).

The effective magnetic field \mathbf{H}_{eff} derives from the functional derivative of the free energy $F(\mathbf{M})$ with respect to \mathbf{M} . For BP an appropriate model $F(\mathbf{M})$ may

be represented in the form [73], [74]

$$F(\mathbf{M}) = \int_V d^3\mathbf{r} \left[\frac{A_s}{2} (\nabla \mathbf{M})^2 + \gamma_1 M^2 + \gamma_2 M^4 - \frac{\mu_0}{2} \mathbf{M} \cdot (\mathbf{H} + \mathbf{H}_{\text{ext}}) \right]. \quad (2)$$

The effective field is

$$\mathbf{H}_{\text{eff}} = -\frac{\delta F}{\delta \mathbf{M}} = \mathbf{H}_{\text{ext}} + \mathbf{H} + \left(\frac{\partial^2}{\partial r^2} + \frac{2}{r} \frac{\partial}{\partial r} - \frac{2}{r^2} \right) \mathbf{M} + 2\nu (\mathbf{M} - \beta \mathbf{M}^3) \quad (3)$$

where A_s is related to the exchange interaction and γ_1, γ_2 are the Landau parameters. We introduce the definitions $\nu = |\gamma_1|/\mu_0$, $\beta = -2\gamma_2/\gamma_1$, and use r as the distance from the global origin, i.e. the center of the BP, to the observation point.

We seek a material-independent formulation but as a typical example we consider here, the helimagnet FeGe for which the exchange stiffness $A = A_s/2$ is $6.1 \cdot 10^{-13} \text{ cm}^2$; the saturation magnetization is $M_s = 383 \text{ emu/cm}^3$, and the Curie temperature is 278.7 K [75]. These parameters vary strongly if we consider a different setting such as spin ice [65, 66].

A. Local magnetic susceptibility

The non-linear coupled equations (1) account for a multitude of phenomena such as large-angle magnetic precession/reversal (magnetic moment quenching is not included in these equations), trapping of electromagnetic waves, and frequency up- and down-conversion. In the linear regime, information on the sample in its field-free state can be obtained. The task here is to derive explicitly an expression for the magnetic permeability matrix of the BP, which as we expect from the above discussion should be frequency dependent and non-local. To this end, we linearize \mathbf{M} with respect to small deviations caused by the external field. We consider a time-independent ground state as the free energy (2) minimum $\mathbf{H}_{\text{eff}} = 0$ [73] and examine small deviations of these ground state solutions under a Landau–Lifshitz–Gilbert formulation. We substitute the expression for the effective magnetic field \mathbf{H}_{eff} into the Landau–Lifshitz–Gilbert equation and write [76]

$$\mathbf{M}(\mathbf{r}, t) = \mathbf{M}_0 + \delta \mathbf{M} = \mathbf{m}_0(\mathbf{r}, t) M_0(r) + \mathbf{m}_1(\mathbf{r}, t) M_0(r). \quad (4)$$

Here, $\mathbf{M}_0(\mathbf{r}, t)$ is the ground state spin configuration which is described by local magnetization magnitude $M_0(r)$ and a unit vector field $\mathbf{m}_0(\mathbf{r}, t)$. Small deviations from the initial configuration are captured by the vector field $\delta \mathbf{M}(\mathbf{r}, t) = \mathbf{m}_1(\mathbf{r}, t) M_0(r)$. To first-order in \mathbf{m}_1 we find

$$\frac{\partial \mathbf{m}_1}{\partial t} = -g\mu_0 M_s [\mathbf{m}_0 \times \mathbf{H}_{\text{eff}}]. \quad (5)$$

In spherical coordinates with the center being at the BP singularity we write

$$\begin{aligned} m_r^0 &= \sin^2 \theta \cos \gamma + \cos^2 \theta, \\ m_\theta^0 &= \cos \theta \sin \theta (\cos \gamma - 1), \\ m_\varphi^0 &= \sin \gamma \sin \theta. \end{aligned} \quad (6)$$

Here γ is a pseudo azimuthal angle which determines the geometry of the spin configuration without changing the topology. For example, for one magnetic singularity at the origin, one transforms from the hedgehog configuration for $\gamma = 0$ to a twisted one for $\gamma = 60^\circ$, where θ is the polar angle between the radial line and the polar z -axis. M_0 is space dependent but still we can normalize to the maximum value of the saturation magnetization M_s , as done in (5), implying $\beta M_s^2 = 1$. We note that no φ -dependence is present and $\mathbf{r} = (\theta, r)$.

For a time-harmonic, polarization structured (vector) EM incident beam we start from (5) and seek the elements of the magnetic permeability matrix $\mu_{ij}(\theta, r) = \delta_{ij} + M_0(r) \chi_{ij}(\theta, r)$ (where $\chi_{i,j}(\theta, r)$ is a magnetic susceptibility $\mathbf{m}_1 = \chi_{i,j}(\mathbf{H} + \mathbf{H}_{\text{eff}})$). It is possible to derive the local element $\chi_{ij}(\theta, r)$ explicitly. The details involve relatively lengthy expressions which are given in Appendix A. Note that the magnetic permeability tensor is Hermitian. As detailed in Appendix A, a key signature of the spin non-collinearity is the appearance of multiple local resonances ω_{res} determined by the condition

$$\begin{aligned} \omega_{\text{res}} &= \pm g\mu_0 M_s [\hat{O} M_0(r)], \\ \hat{O} &= \left(\frac{\partial^2}{\partial r^2} + \frac{2}{r} \frac{\partial}{\partial r} - \frac{2}{r^2} \right) + 2\nu (1 - M_0^2). \end{aligned} \quad (7)$$

Importantly, this fact can be exploited to sense for BPs in the frequency space without being hindered by the limited spatial resolution of optical probes.

B. Scattering of electromagnetic fields: Spherical coupled-wave analysis

To calculate the scattered fields from localized magnetic non-collinearities, we formulate a spherical rigorous coupled-wave analysis by dividing the sphere around the magnetic singularity into onion-type, thin shell layers, where the l -th thin layer ($l = 1 \dots L$) is characterized by a magnetic permeability matrix $\mu_{ij}(\theta, r_l)$ (c.f. an inset in Fig. 1). Here, r_l is the radial distance of the l -th thin shell layer and all material parameters are assumed to be constant within each layer. It is important to mention that each shell layer resonates at a different frequency defined by (7). Hence, the magneto-optical behavior under irradiation with a broadband vector beam, such as suggested in [77], will be qualitatively different from a homogeneous beam. For the numerical demonstration we choose the excitation frequency ω close to the resonance frequency of

the outermost shell layer, i.e. $\omega_{res}(r = a)$. This means that the elements of the magnetic permeability matrix attain maximum values in the outermost layer and then decrease within the BP when approaching its global origin (detailed derivation is given in Appendix A).

Having the magnetic permeability matrix rigorously derived, we then substitute it into the Maxwell's equations written in spherical coordinates and redefine the components of the electric E_r^α and magnetic H_r^α fields as

$$S_\theta^\alpha = r E_\theta^\alpha, S_\varphi^\alpha = r \sin \theta E_\varphi^\alpha,$$

$$U_\theta^\alpha = \sqrt{\mu_0/\epsilon_0} r H_\theta^\alpha, U_\varphi^\alpha = \sqrt{\mu_0/\epsilon_0} r \sin \theta H_\varphi^\alpha,$$

where $\alpha = inc, r$ represents the incident or reflected fields. By expanding the fields into a one-dimensional (1-D) Fourier series with respect to a parameter $\kappa = \cos \theta$ ($\theta = [0 : \pi]$) [78, 79]:

$$\Phi(r, \theta) = \sum_{i=-N}^N \phi_i(r) e^{j i \pi \kappa}, \quad \Phi = \{S_\theta, S_\varphi, U_\theta, U_\varphi\} \quad (8)$$

a set of first-order, coupled differential equations for the radially varying field amplitudes $\phi_i(r) = [s_\theta^i, s_\varphi^i, u_\theta^i, u_\varphi^i]$ is obtained:

$$\frac{d}{d\eta} \begin{bmatrix} s_\theta^i \\ s_\varphi^i \\ u_\theta^i \\ u_\varphi^i \end{bmatrix} = j [\Psi] = j \begin{bmatrix} \Psi_{11} & \Psi_{12} & \Psi_{13} & \Psi_{14} \\ \Psi_{21} & \Psi_{22} & \Psi_{23} & \Psi_{24} \\ \Psi_{31} & \Psi_{32} & \Psi_{33} & \Psi_{34} \\ \Psi_{41} & \Psi_{42} & \Psi_{43} & \Psi_{44} \end{bmatrix} \begin{bmatrix} s_\theta^i \\ s_\varphi^i \\ u_\theta^i \\ u_\varphi^i \end{bmatrix}. \quad (9)$$

Here $\eta = k_0 r$, k_0 is the free-space wavenumber, N is a truncation number of the Fourier series that will be varied to check convergence, Ψ is a square matrix generated by the Fourier coefficients of $\Psi_{qq'}$ with the (n, m) entries equal to $\Psi_{qq'}^{n-m}$. If a truncation number for each field component associated with the Fourier series is N , $(-N \dots 0 \dots N)$, then the size of the matrix Ψ becomes $4(2N+1) \times 4(2N+1)$. The implicit expressions of block matrices $\Psi_{qq'}$ are given in Appendix B.

Using (9), the fields for each anisotropic layer are expressed through the eigenvectors and eigenvalues of the matrix Ψ . Hence, the tangential components of the electric and magnetic fields in the l -th shell layer characterized by a normalized radial distance $\eta_l = k_0 r_l$, namely $(S_\theta^{(l)}(\kappa, \eta_l), S_\varphi^{(l)}(\kappa, \eta_l))$ and $(U_\theta^{(l)}(\kappa, \eta_l), U_\varphi^{(l)}(\kappa, \eta_l))$, can be written in the following form:

$$\begin{aligned} \mathbf{S}^{(l)}(\kappa, \eta_l) &= \sum_{i=-N}^N \left(\sum_{p=1}^{4(2N+1)} P_{ip,U}^{(l)} e^{j \eta_l |\xi_p^l|} C_p^{(l)} \right) e^{j i \pi \kappa} \\ &= \sum_{i=-N}^N \left(\bar{\bar{\mathbf{P}}}^{(l)}_U \cdot \mathbf{\Upsilon} \cdot \mathbf{C}^{(l)} \right) e^{j i \pi \kappa}. \end{aligned} \quad (10)$$

$$\begin{aligned} \mathbf{U}^{(l)}(\kappa, \eta_l) &= \sum_{i=-N}^N \left(\sum_{p=1}^{4(2N+1)} P_{ip,U}^{(l)} e^{j \eta_l |\xi_p^l|} C_p^{(l)} \right) e^{j i \pi \kappa} \\ &= \sum_{i=-N}^N \left(\bar{\bar{\mathbf{P}}}^{(l)}_U \cdot \mathbf{\Upsilon} \cdot \mathbf{C}^{(l)} \right) e^{j i \pi \kappa}. \end{aligned} \quad (11)$$

where we introduced the shorthand notation

$$\mathbf{S}^{(l)}(\kappa, \eta_l) = [S_\theta^{(l)}(\kappa, \eta_l), S_\varphi^{(l)}(\kappa, \eta_l)]^T, \quad (12)$$

$$\mathbf{U}^{(l)}(\kappa, \eta_l) = [U_\theta^{(l)}(\kappa, \eta_l), U_\varphi^{(l)}(\kappa, \eta_l)]^T. \quad (13)$$

Here, the matrices $\bar{\bar{\mathbf{P}}}^{(l)}_S$ and $\bar{\bar{\mathbf{P}}}^{(l)}_U$ having a size $2(2N+1) \times 4(2N+1)$ are constructed from the eigenvectors of the matrix Ψ^l in the l -th shell layer. $\{\xi_p^l\}$ determine the elements of the diagonal matrix $\mathbf{\Upsilon}$ and are set by the respective eigenvalues of Ψ^l .

A relation between the unknown coefficients $\mathbf{C}^{(l)}$ and $\mathbf{C}^{(l-1)}$ in the l -th and $(l-1)$ -th shell layers, respectively, is determined by the boundary conditions for the incoming and outgoing waves on the l -th layer's boundary

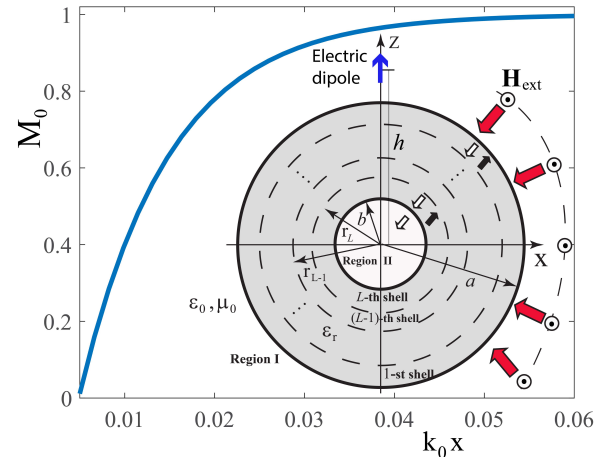


Figure 1. Curve showing the normalized magnetization M_0 as a function of $k_0 x$, where k_0 is the free-space wavenumber. Inset shows a schematic cross-sectional view of the BP, where the magnetic order is spherically surrounding the BP. The outer-radius of the sphere is a and the inner-radius is denoted as b . The anisotropic region (see Appendix A) is marked by the gray color. It is divided into thin shell layers, each of which is characterized by the local magnetic permeability matrix $\mu_{ij}(\theta, r_l)$. Outside the anisotropic structure the medium is assumed to be free space. The relative dielectric permittivity of the spherical BP is ϵ_r . The wavefront of the incident field is also depicted by thick red arrows. The direction of the associated magnetic field \mathbf{H}_{ext} is indicated by dotted circles. Such a field can be realized by a radially directed elementary electric dipole which is marked by a blue arrow and is located on and parallel to the z -axis at a distance h from the global origin (i.e., the center of the BP).

[79, 80]:

$$\mathbf{C}^{(l)} = [\bar{\mathbf{P}}_S^{(l)}, \bar{\mathbf{P}}_U^{(l)}]^T \cdot \mathbf{P}^{(l-1)} \cdot \mathbf{T}^{(l-1)} \cdot \mathbf{C}^{(l-1)} \equiv \mathbf{F}^l \cdot \mathbf{C}^{(l-1)} \quad (14)$$

Here $\mathbf{P}^{(l)} = [\bar{\mathbf{P}}_S^{(l)}, \bar{\mathbf{P}}_U^{(l)}]^T$ is a square matrix (its size is $4(2N+1) \times 4(2N+1)$) whose columns are the eigenvectors of the matrix Ψ^l in the l -th shell layer, $\mathbf{T}^{(l-1)}$ is related to the thickness of the $(l-1)$ -th thin shell and represents the traveling wave behavior of the space-harmonics along the radial direction. Since the relationship between the coefficients for the adjacent layers inside the sphere have been determined, the relation between $\mathbf{C}^{(1)}$ in the outermost 1-st layer inside the sphere (the nearest one to the region of an incident wave) and $\mathbf{C}^{(L)}$ in the innermost L -th layer (the closest one to the global origin) can be calculated using a recursive algorithm based on the matrix multiplication: $\mathbf{C}^{(L)} = \mathbf{F} \cdot \mathbf{C}^{(1)}$. The matrix \mathbf{F} , which is a product of matrices \mathbf{F}^l ($l = 1 \dots L$), rigorously accounts for multiple interaction of the space-harmonics between the shell layers, as well as their material and geometrical parameters through the eigenvectors and eigenvalues of the Ψ^l matrix.

The electromagnetic fields in the space $r > a$, i.e., Region I in the inset of Fig. 1, are expressed in terms of transverse to r electric (TE_r) and transverse to r magnetic (TM_r) waves and may be written using Schelkunoff-Bessel and Hankel functions in the following form:

$$S_\theta^{(I)}(r, \kappa) = \sum_{i=-N}^N (\mathbf{K} \cdot \mathbf{c}) e^{j i \pi \kappa} + \sum_{i=-N}^N S_{\theta, i}^{\text{inc}} e^{j i \pi \kappa} \quad (15a)$$

$$S_\varphi^{(I)}(r, \kappa) = - \sum_{i=-N}^N (\tilde{\mathbf{K}} \cdot \mathbf{d}) e^{j i \pi \kappa} + \sum_{i=-N}^N S_{\varphi, i}^{\text{inc}} e^{j i \pi \kappa} \quad (15b)$$

$$U_\theta^{(I)}(r, \kappa) = \sum_{i=-N}^N (\mathbf{K} \cdot \mathbf{d}) e^{j i \pi \kappa} + \sum_{i=-N}^N U_{\theta, i}^{\text{inc}} e^{j i \pi \kappa} \quad (15c)$$

$$U_\varphi^{(I)}(r, \kappa) = \sum_{i=-N}^N (\tilde{\mathbf{K}} \cdot \mathbf{c}) e^{j i \pi \kappa} + \sum_{i=-N}^N U_{\varphi, i}^{\text{inc}} e^{j i \pi \kappa} \quad (15d)$$

with

$$\mathbf{K} = \{K_{in}\} = j g_{in} \hat{h}_n^{(2)'}(\eta), \quad (16)$$

$$\tilde{\mathbf{K}} = \{\tilde{K}_{in}\} = \tilde{g}_{in} \hat{h}_n^{(2)}(\eta), \quad (17)$$

$$g_{in} = \frac{1}{2} \int_{-1}^1 d\kappa \sqrt{1 - \kappa^2} \frac{dP_n^0(\kappa)}{d\kappa} e^{-j i \pi \kappa}, \quad (18)$$

$$\tilde{g}_{in} = \frac{1}{2} \int_{-1}^1 d\kappa (1 - \kappa^2) \frac{dP_n^0(\kappa)}{d\kappa} e^{-j i \pi \kappa}. \quad (19)$$

Here $P_n^0(\kappa)$ are the associated Legendre polynomials, $\hat{h}_n^{(2)}(\eta)$ are the Schelkunoff Hankel functions of the second kind satisfying the radiation condition and the prime denotes differentiation with respect to the argument. \mathbf{c} and \mathbf{d} are the scattering amplitudes that should be determined by matching the boundary conditions at $r = a$. The first terms on the right side in (15a)-(15d) represent the reflected waves, whereas the second terms are the incident waves. The i -th Fourier component of the radial electric and magnetic fields can be written as

$$e_r^i = -i\pi(k_0/\eta^2)u_\varphi^i, \quad h_r^i = i\pi(k_0/\eta^2)\sqrt{\epsilon_0/\mu_0}s_\varphi^i.$$

Equations (15a) - (15d) are written in a general form. The formalism does not pose any restrictions on the position or nature of the excitation sources, meaning structured light optical vortices, vector beams [81] and optical skyrmions can serve as inputs [82-84]. What is needed for a given input field is the expansion of the incident field and the scattered fields in the surrounding space (i.e., Region I) as well as inside the magnetically ordered materials in terms of the same basis which allows the boundary conditions on the surfaces of the sphere to be matched. More details are provided in Appendix C. Without loss of generality in this work we analyze only the lowest-order spherical waves generated by elementary sources as shown in (C1) and (C2) of Appendix C. To emphasize the generality of the formalism, in Appendix C we briefly describe also an implementation of radially and azimuthally polarized beams. It is established that the sum of the radially and azimuthally polarized beams produce a circularly polarized vortex beam which is used to probe the magnetic vortex dynamics [64].

In our previous works for periodic planar geometries [80, 85, 86] we expanded the fields into a set of space harmonics varying as $e^{jk_{xn}x}$, where k_{xn} are the wavenumbers along the periodicity (along the x -axis). Here, however, we are dealing with the spherical symmetry and therefore, we need to use the fields' expansion in terms of the polar θ angle (meaning in the basis of $e^{j i \pi \kappa}$).

At the singularity, the magnetic moment and hence the scattering from it vanishes. To deal with this region numerically, we define the fields at $r = 0$ that appear in the denominator of the block matrices in Appendix B, and a small homogeneous spherical region surrounding the global origin and having a radius b is considered. It is denoted as Region II (c.f. inset in Fig. 1) and without loss of generality is assumed to be the dielectric background space. The fields in Region II can be written in a similar form as those in Region I. The main difference is that instead of the Schelkunoff Hankel function $\hat{h}_n^{(2)}(\eta)$ we will have a standing wave that is expressed by the Schelkunoff Bessel function $\hat{j}_n(\eta)$. This is because an incoming wave $\hat{h}_n^{(1)}(\eta)$ is completely reflected at the global origin thus generating $\hat{h}_n^{(2)}(\eta)$, which leads to the formation of the total field - the standing wave

$\hat{j}_n(\eta) = 0.5[\hat{h}_n^{(1)}(\eta) + \hat{h}_n^{(2)}(\eta)]$ - in Region II [87]. This significantly differs from the analysis for the planar geometry [80, 85, 88], where the transmitted field in the innermost region is represented in terms of incoming plane waves. Moreover, there are no incident fields in Region II and hence, the last terms on the right side in (15a)-(15d) should be set to zero.

Finally, by matching the boundary conditions at $r = a$ and $r = b$, we obtain the following two equations from which the unknown $\mathbf{C}^{(1)}$ can be determined

$$\begin{aligned} \left[\bar{\bar{\mathbf{P}}}^{(1)}_U - \begin{pmatrix} \mathbf{K} & 0 \\ 0 & \tilde{\mathbf{K}} \end{pmatrix} \begin{pmatrix} 0 & \mathbf{K} \\ -\tilde{\mathbf{K}} & 0 \end{pmatrix}^{-1} \bar{\bar{\mathbf{P}}}^{(1)}_S \right] \mathbf{C}^{(1)} = \\ = \begin{pmatrix} \mathbf{U}_\theta^{inc} \\ \mathbf{U}_\varphi^{inc} \end{pmatrix} - \begin{pmatrix} \mathbf{K} & 0 \\ 0 & \tilde{\mathbf{K}} \end{pmatrix} \begin{pmatrix} 0 & \mathbf{K} \\ -\tilde{\mathbf{K}} & 0 \end{pmatrix}^{-1} \begin{pmatrix} \mathbf{S}_\theta^{inc} \\ \mathbf{S}_\varphi^{inc} \end{pmatrix} \end{aligned} \quad (20)$$

$$\left[\bar{\bar{\mathbf{P}}}^{(L)}_U - \begin{pmatrix} \mathbf{G} & 0 \\ 0 & \tilde{\mathbf{G}} \end{pmatrix} \begin{pmatrix} 0 & \mathbf{G} \\ -\tilde{\mathbf{G}} & 0 \end{pmatrix}^{-1} \bar{\bar{\mathbf{P}}}^{(L)}_S \right] \mathbf{C}^{(L)} = 0 \quad (21)$$

with

$$\mathbf{G} = \{G_{in}\} = jg_{in}\hat{j}'_n(\eta), \quad \tilde{\mathbf{G}} = \{\tilde{G}_{in}\} = \hat{g}_{in}\hat{j}_n(\eta). \quad (22)$$

Once $\mathbf{C}^{(1)}$ is found, the fields inside (using (10) and (11) together with (14)), as well as outside (using (15a) - (19)) the BP are fully determined.

III. NUMERICAL RESULTS AND DISCUSSIONS

To validate the correctness and accuracy of the proposed formalism we begin by studying two relatively simple models of electromagnetic scattering of the spherical transverse magnetic TM_r and transverse electric TE_r incident waves on: a) a homogeneous dielectric sphere, and b) a dielectric sphere with radially varying relative dielectric permittivities. The results are then compared with analytical solutions obtained based on the 3-D transition matrix (T-matrix) theory [87] which utilizes the expressions for the fields in terms of spherical functions in all regions. The results are not shown here for brevity, however, very good agreement is found for all cases. Note that for a homogeneous scatterer the fields are decoupled and only a set of two differential equations for $(E_r, S_\theta, U_\varphi)$ corresponding to the TM_r wave and $(H_r, U_\theta, S_\varphi)$ corresponding to the TE_r wave are solved separately. This is not the case for the analysis of the BPs, which is characterized by the magnetic permeability matrix. Therefore, a set of four coupled differential equations have to be solved, as shown in Appendix B.

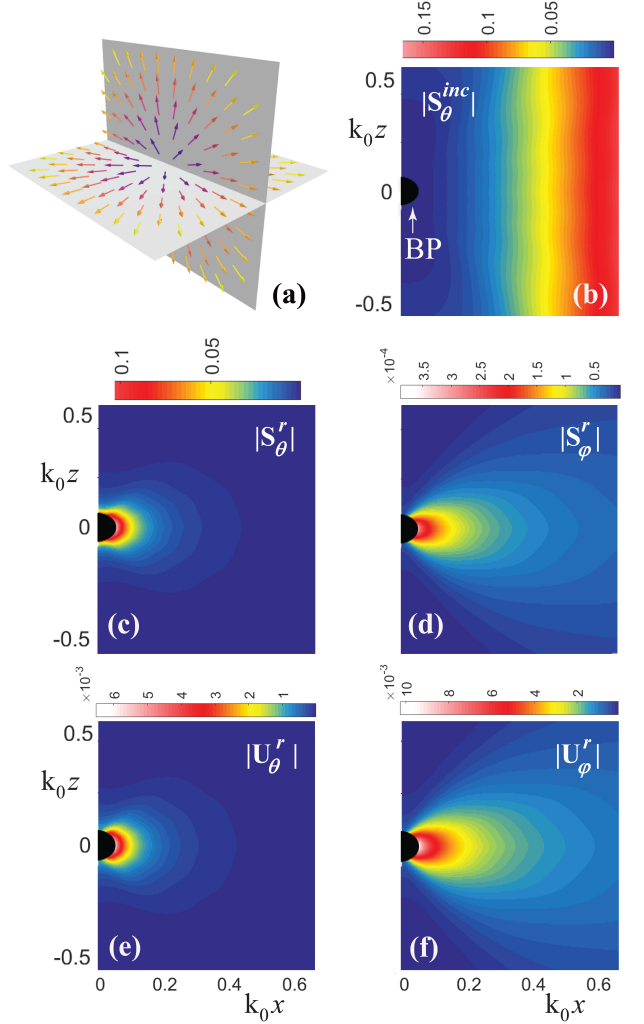


Figure 2. (a) The hedgehog Bloch point ($\gamma = 0^0$); (b) the incident electric fields $|S_\theta^{inc}|$; (c), (d) the reflected electric fields $|S_\theta^r|$ and $|S_\varphi^r|$, respectively; (e),(f) the reflected magnetic fields $|U_\theta^r|$ and $|U_\varphi^r|$, respectively. Here $k_0a = 0.06$, $k_0b = 0.005$, $\epsilon_r = 12$ and $k_0h = 4$.

1. Hedgehog magnetic texture

As the simplest interesting example, consider an electric dipole radiation source positioned on the z -axis and pointing along it (see Fig.1). This source radiates the lowest-order spherical waves expressed by a zero-th order spherical Hankel function [89] (see Appendix C). The only non-zero components of the incident field produced by this elementary dipole are U_φ^{inc} , S_r^{inc} and S_θ^{inc} (these field components are derived from the expression for the radially directed magnetic vector potential). Hence, the second terms on the right-hand side in (15b) and (15c) are set to zero. Although our formalism is general, in this paper we consider a relatively simple model, when there is not a magnetic material beyond the BP and the source is located in the free space

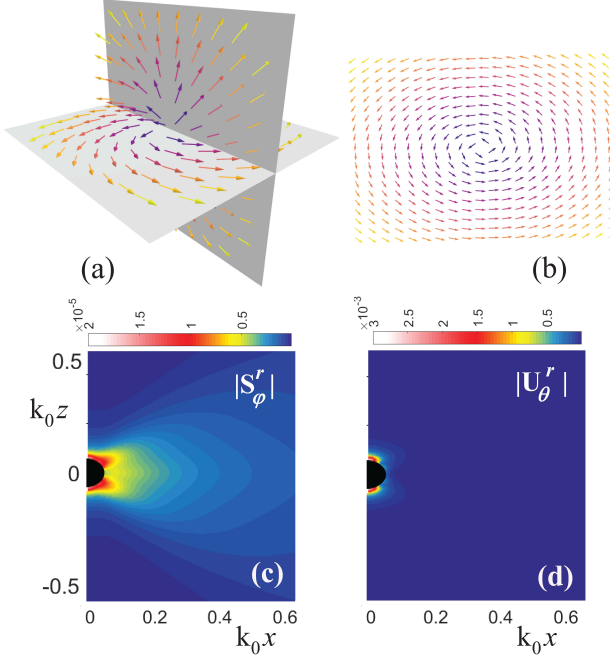


Figure 3. (a) The twisted BP; (b) its projection on the equatorial cut ($\theta = 90^\circ$); (c),(d) the spatial distributions of the reflected electric $|S_\varphi^r|$ and magnetic $|U_\theta^r|$ fields, respectively. The other parameters are the same as those in Fig. 2.

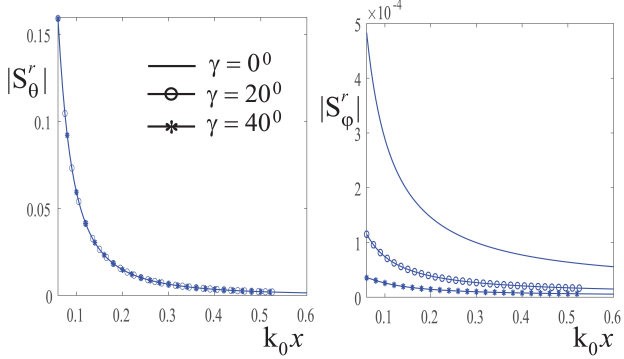


Figure 4. The reflected electric field components $|S_\theta^r|$ (left figure) and $|S_\varphi^r|$ (right figure) versus k_0x at a fixed polar angle $\theta = 90^\circ$ for different azimuthal rotation angles γ : $\gamma = 0^\circ$ (solid line); $\gamma = 20^\circ$ (circles); $\gamma = 40^\circ$ (asterisk). The other parameters are the same as those in Fig. 2.

surrounding the BP. The goal of this paper is to capture the physics of BP and present fundamental studies about its interaction with the incoming spherical wave, i.e. to study how the fields are modified by the singular magnetic texture. The present approach allows, in principle, to study bulk and interfaces with regard to dielectric as well as to background-magnetic properties.

Firstly, a hedgehog Bloch point ($\gamma = 0^\circ$), when the unit vectors of magnetization inside the BP have only radial components ($m_r^0 \neq 0$, $m_\theta = m_\varphi = 0$), is con-

sidered (c.f. Fig. 2(a)). This structure can be viewed as an emergent magnetic monopole. After several tests for convergence of the solutions, the truncation number was chosen as $N = 5$. The BP is divided into 25 equal thin shell layers and all material parameters are assumed to be constant within each thin shell layer (see Sec. II). The absolute value of the incident electric field $|S_\theta^{inc}|$ and the reflected electric $|S_\theta^r|$, $|S_\varphi^r|$ and magnetic $|U_\theta^r|$, $|U_\varphi^r|$ fields are demonstrated in Figs. 2(b) - 2(f) at $k_0a = 0.06$, $k_0b = 0.005$, $\epsilon_r = 12$ and $k_0h = 4$. In this work we develop a general, material-independent formulation, and do not specify a particular material. However, we should note that the radius of the sphere a should be taken to be much smaller than the wavelength, since the electromagnetic waves are in the range of magnetic excitations. The formalism analytically and numerically is not restricted to a particular location of the source. Here, the dipole is chosen to be located at a relatively large distance from the BP and hence, the incident wavefront impinging on the BP has a symmetric profile with respect to the polar θ angle (for a dipole source closer to the BP, the field would lose its symmetric profile and would be concentrated in the vicinity of the upper half of the sphere). The reflected fields show typical profiles with strong localization in the vicinity of the BP at around $\theta = 90^\circ$ and the θ -components of both fields decrease faster than the φ -components with increasing a distance from the surface of the BPs.

2. Twisted Bloch point

Let us consider the effect of the azimuthal rotation angle γ generating twisted BP in Fig. 3(a) on the EM wave scattering. Unlike the hedgehog BP, in the case of the twisted BP at $\gamma \neq 0$, the unit vector of magnetization is radially oriented only at the poles of $\theta = 0^\circ$ and $\theta = 180^\circ$. Its orientation as a function of θ is defined by (6). Let us inspect the field distributions of $|U_\theta^r|$ and $|S_\varphi^r|$ at $\gamma = 60^\circ$. These field components are excited solely by an interaction of the incident field with the BP and contribute to a formation of the scattered fields, in particular they are not present in the incident field, i.e., $S_\varphi^{inc} = U_\theta^{inc} = 0$. The results of the field distributions are given in Figs. 3(b) and 3(c). From the figures it follows that the field distributions for $|S_\varphi^r|$ and $|U_\theta^r|$ exhibit quite different profiles from those in Figs. 2(d) and 2(e). The fields are no longer localized at around $\theta = 90^\circ$, but are concentrated closer to the z -axis of the twisted BP. The results are not shown, but interestingly, S_θ^r and U_φ^r do not show any changes from those in Figs. 3(c) and 3(f) at $\gamma = 0^\circ$. To study this phenomenon in more detail, $|S_\theta^r|$ and $|S_\varphi^r|$ are plotted as a function of k_0x at a fixed spherical angle $\theta = 90^\circ$ for different values of γ : $\gamma = 0^\circ$ (solid line); $\gamma = 20^\circ$ (circles); $\gamma = 40^\circ$ (asterisk). The results of the reflected electric fields are illustrated in Fig. 4. As expected, S_θ^r (black line) does not show any changes when increasing

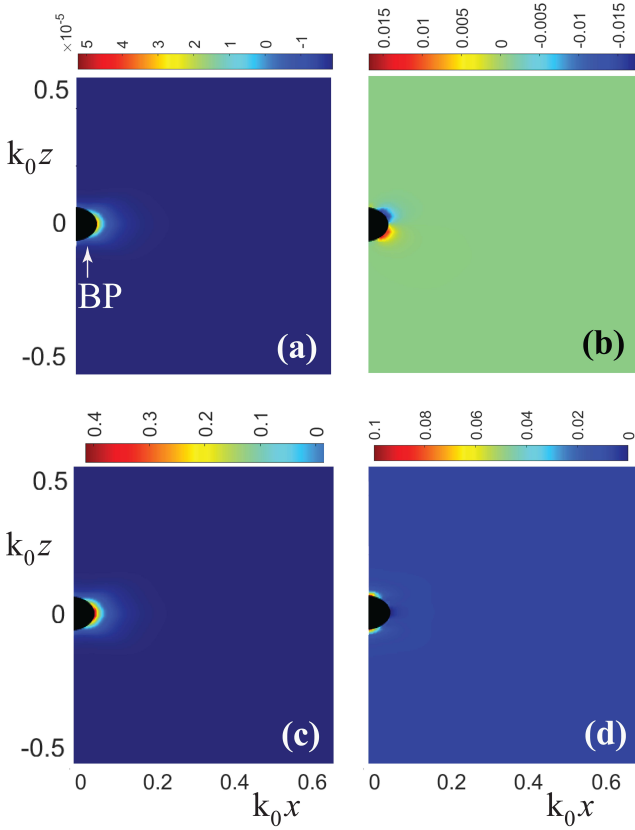


Figure 5. (a), (b): Time-averaged gauge-invariant optical chiral density and (c),(d): the magnetoelectric density for the hedgehog Bloch point (left figures) and the twisted Bloch point $\gamma = 60^\circ$ (right figures). The other parameters are the same as in Fig. 2.

γ , whereas a maximum of S_φ^r (red line) is decreasing inversely proportional to γ . The results for the magnetic field show similar profiles. Namely, U_φ^r is not changing by increasing γ .

3. Emergent features of formed EM fields and magnetoelectric coupling

Having shown how the noncollinear magnetic texture mold the incoming EM waves, it is of interest to consider the specific features of these fields. Here, several well-established quantities will be discussed. The time-average of the important magnetoelectric pseudoscalar $\mathbf{E} \cdot \mathbf{H}$ may be expressed as $Q_{ME} = \mathbf{E} \cdot \mathbf{H} = \frac{1}{2} \left[S_\theta U_\theta^* + \frac{S_\varphi U_\varphi^*}{1-\kappa^2} - \frac{1}{\eta^2} \frac{\partial U_\varphi}{\partial \kappa} \left(\frac{\partial S_\varphi}{\partial \kappa} \right)^* \right]$ from which the time-averaged, normalized (propagating) optical chiral density χ follows as [90]:

$$\chi = \frac{1}{\eta^2} \Im(Q_{ME}), \quad (23)$$

and the reactive magnetoelectric density A_{ME} is [91] $A_{ME} = \frac{1}{\eta^2} \Re(Q_{ME})$. Q_{ME} is derived directly from the

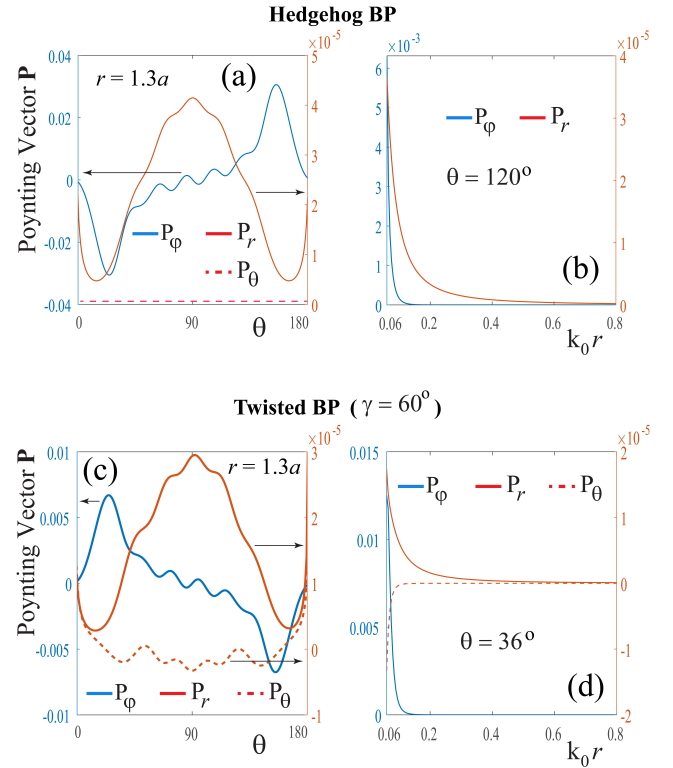


Figure 6. Time-averaged Poynting vector of the reflected fields as a function of (a): the polar angle θ at the fixed radial distance $r = 1.3a$, i.e. very close to the outer surface of the hedgehog BP; (b) the normalized radial distance $k_0 r$ at the spherical cut $\theta = 120^\circ$. (c),(d): the same as above but for the twisted BP at $\gamma = 60^\circ$.

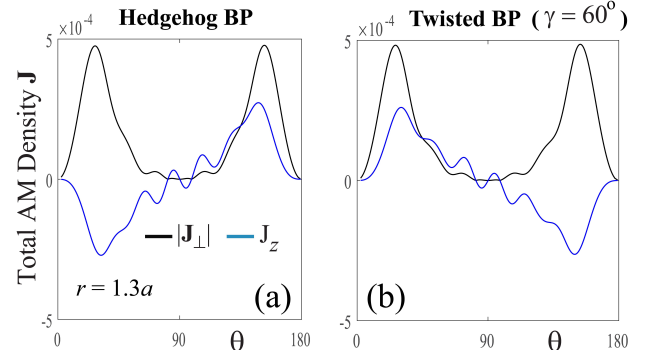


Figure 7. Total angular momentum (AM) density $|\mathbf{J}_\perp|$ (black line) and J_z (blue line) as a function of the polar angle θ at the fixed radial distance $r = 1.3a$ for: (a) the hedgehog BP; (b) the twisted BP.

fields and hence χ and A_{ME} are gauge-invariant. These values are normalized by $\epsilon_0 k_0^3/2$. Here, we recall the importance of producing fields with time-averaged, finite and possibly tunable $\mathbf{E} \cdot \mathbf{H}$ for research concerning chiral materials [92], axion fields in general, and axion electrodynamics of a 3-D topological insulator in particular as well as to access spin-charge response in

condensed matter [93–96]. Our results for χ and A_{ME} in Fig. 5 for hedgehog and twisted BPs are generated by fields determined using (8). Irradiating with fields having no χ and A_{ME} , meaning any transverse fields with real-valued \mathbf{E} , upon interaction with the magnetic texture, the phases and the directions of \mathbf{E} and \mathbf{H} are mixed leading to a formation of localized finite χ and A_{ME} . The twist in a BP allows for more channels for scattering and hence more mixing enhancing the maximal magnitude of χ and A_{ME} . The strong localization of the produced magnetoelectric activity implies that if we have a collection of BP-type textures, as they occur for example in artificial spin ice or gyroid structures [67], then a lattice of χ and A_{ME} will be formed. Notably, $\mathbf{E} \cdot \mathbf{H}$ has been observed experimentally in the center of plasmonic vortices [97]. The method identified here generates finite, time averaged χ and A_{ME} in a non-dissipative way and they are localized well beyond the BPs, whereas in plasmonic-based methods χ and A_{ME} live at the metal-dielectric interface. Thus, our scheme is qualitatively different and complementary to the plasmonic method. This remark becomes relevant when using χ and A_{ME} to probe unperturbed samples.

For optical forces and torques as well as for an insight into the energy flow and the orbital angular momentum distribution, the components of the time-averaged Poynting vector \mathbf{P} are important. They are calculated according to the following expressions:

$$\begin{aligned} P_r &= \frac{1}{2\eta^2\sqrt{1-\kappa^2}} \Re(S_\theta U_\varphi^* - S_\varphi U_\theta^*), \\ P_\theta &= \frac{1}{2\eta^3\sqrt{1-\kappa^2}} \Re\left(\frac{U_\varphi^*}{j} \frac{\partial U_\varphi}{\partial \kappa} + S_\varphi \left(\frac{1}{j} \frac{\partial S_\varphi}{\partial \kappa}\right)^*\right), \\ P_\varphi &= \frac{1}{2\eta^3\sqrt{1-\kappa^2}} \Re\left(-\frac{U_\theta^*}{j} \frac{\partial U_\varphi}{\partial \kappa} - S_\theta \left(\frac{1}{j} \frac{\partial S_\varphi}{\partial \kappa}\right)^*\right). \end{aligned} \quad (24)$$

These components are shown in Figs. 6(a) and 6(c) for the hedgehog BP and the twisted BP as a function of θ at a fixed radial distance $r = 1.3a$ close to the outer surface. The Poynting vector components are normalized by $k_0^2 \sqrt{\epsilon_0/\mu_0}$. The main contribution is carried by P_φ (blue line) which is antisymmetric with respect to the equatorial cut $\theta = 90^\circ$. We recall that P_φ is the only component of the Poynting vector which is predominantly influenced by an interaction of the electromagnetic wave with the BP (as inferred from the third expression in (24) which indicates that $P_\varphi = 0$ if the magneto-optical activity of the BP disappears). Further numerical results and analysis evidence that the shape of P_φ , as expected, does not show any substantial variations with respect to the radial distance r (in particular its antisymmetric profile is not changing). Another point worth noticing is that unlike the hedgehog BP, the θ component of the Poynting vector is more pronounced for the twisted BP (red dashed line). As for

the radial component of the Poynting vector P_r , similar profiles (red line) are exhibited for both types of BPs. Note that the radial component of the Poynting vector is mainly affected by the homogeneous dielectric permittivity of the scatterer and is not sensitive to the elements of the magnetic permeability matrix that characterize the BP. Assuming $g\mu_0 M_s = 0$ one readily concludes that all non-diagonal components of the permeability matrix in Appendix A become zero and the diagonal components are equal to unity. Dependence of the Poynting vector components versus the normalized radial distance $k_0 r$ in some particular spherical cuts is shown in Figs. 6(b) and 6(d). The P_φ and P_θ components are rapidly decreasing in magnitudes as the radial distance grows but are localized clearly outside the BPs. In the far-field region (with respect to the BP size) only the radial component of the Poynting vector survives, as expected for EM wave scattering by homogeneous objects.

Generally, the total angular momentum density follows from $\mathbf{J} = \mathbf{r} \times \mathbf{P}/c^2$. For strongly non-paraxial beams, it is not unique how the orbital angular momentum density \mathbf{L} can be disentangled from the spin angular momentum density \mathbf{S} as is done in [98] for paraxial beams ($\mathbf{L} = \mathbf{J} - \mathbf{S}$). Hence, we will discuss here \mathbf{J} , keeping in mind that it encompasses both \mathbf{L} and \mathbf{S} . The transversal $|\mathbf{J}_\perp| = \sqrt{J_x^2 + J_y^2}$ and the longitudinal J_z components of the total angular momentum (AM) density are given by

$$|\mathbf{J}_\perp| = \sqrt{\kappa^2 J_\theta^2 + J_\varphi^2}, \quad J_z = -\sqrt{1-\kappa^2} J_\theta \quad (25)$$

with $J_\theta = -r P_\varphi$ and $J_\varphi = r P_\theta$, where r is taken with respect to the global origin. The total AM density $|\mathbf{J}_\perp|$ (black line) and J_z (blue line) as a function of the polar angle θ at the fixed radial distance $r = 1.3a$ for the hedgehog BP and for the twisted BP are shown in Figs. 7(a) and 7(b), respectively. Obviously, in the absence of the magneto-optical effects characterizing the BP, $P_\varphi = 0$, i.e. $J_\theta = 0$ and hence, no total AM density along the z -axis is observed. As for the total AM, i.e. an integration with respect to r and θ , under our prescribed geometrical parameters and the incident field, it will be equal to zero. For a source closer to the BP, the reflected field is substantially stronger, concentrated in the vicinity of the upper half of a sphere enclosing the BP, and a finite total AM results. Finally, we note that some experimental studies for the chiral fields and orbital angular momentum-dependent responses are described in [99]. They can be useful for the analysis of the reflected fields by the BP discussed in this paper, which possess orbital angular momentum, chirality as well as magnetoelectric densities.

IV. CONCLUSIONS

The work presents an efficient and self-consistent approach for the analysis of EM wave scattering by hedgehog and twisted BPs. The goal was to investigate how non-collinear magnetic textures respond to EM fields in the frequency range of magnetic excitations and how to use BPs as photonic elements that modify the scattered (reflected) fields. The formalism is general and can be applied to various excitation sources and spin configurations apart from BPs. Special attention is paid to field components generated solely by an interaction of EM waves and BPs and to their modifications when transforming from a hedgehog to a twisted configuration. The field's spatial distributions, chirality density, magnetoelectric density, Poynting vector, and total angular momentum density are numerically evaluated and analyzed.

The generalization of the formalism to the problem with both θ and φ -dependent spherical objects is straightforward and requires developing explicit expressions for the field components (including the $\partial/\partial\varphi$ terms) in a spherical coordinate system satisfying the vector Helmholtz equation. As a result, the size of the matrix to be solved becomes larger than in the problem considered here, but the analytical procedure remains the same. Finally, it is important to mention that our EM simulations are carried out for a particular size of the BP, the extent to which depends on the temperature T [100]. For a fixed temperature, for example, near the Curie temperature T_c the BP radius scales as $\propto (T - T_c)^{-1/2}$.

AUTHOR CONTRIBUTIONS

All authors equally contributed to this work.

ACKNOWLEDGMENTS

The work has been supported by the Shota Rustaveli National Science Foundation of Georgia (SRNSFG) [FR-23-249] and the DFG under project Nr. 429194455, and DOE (USA) Nr. DE-FOA-0002514. D.E. and V.J. also acknowledge the partial support by the Deutsche Forschungsgemeinschaft (DFG) in the Framework of the CRC/TRR 196 MARIE (Project-ID 287022738) within project M03.

V. Jandieri would like to express his sincere gratitude to Professor Kiyotoshi Yasumoto from Kyushu University, Japan for discussions about the theory of periodic and bandgap structures.

CONFLICT OF INTEREST

The authors declare no potential conflicts of interest.

DATA AVAILABILITY STATEMENT

The data beyond those in the text are available from the authors upon reasonable request.

Appendix A: Magnetic Permeability Matrix

The elements of the magnetic permeability matrix: $\mu_{ij}(\theta, r) = \begin{bmatrix} \mu_{11} & \mu_{12} & \mu_{13} \\ \mu_{12}^* & \mu_{22} & \mu_{23} \\ \mu_{13}^* & \mu_{23}^* & \mu_{33} \end{bmatrix}$ are implicitly written in the following form:

$$\mu_{11} = 1 + \alpha \frac{g^2 \mu_0^2 M_s^2}{\omega^2} ((m_\theta^0)^2 + (m_\phi^0)^2) [\hat{O}M_0(r)], \quad \mu_{12} = \alpha \left(-\frac{g^2 \mu_0^2 M_s^2}{\omega^2} m_r^0 m_\theta^0 [\hat{O}M_0(r)] - j \frac{g \mu_0 M_s}{\omega} m_\phi^0 \right), \quad (A1)$$

$$\mu_{13} = \alpha \left(-\frac{g^2 \mu_0^2 M_s^2}{\omega^2} m_r^0 m_\phi^0 [\hat{O}M_0(r)] + j \frac{g \mu_0 M_s}{\omega} m_\theta^0 \right), \quad \mu_{22} = 1 + \alpha \frac{g^2 \mu_0^2 M_s^2}{\omega^2} ((m_r^0)^2 + (m_\phi^0)^2) [\hat{O}M_0(r)], \quad (A2)$$

$$\mu_{23} = \alpha \left(-\frac{g^2 \mu_0^2 M_s^2}{\omega^2} m_\theta^0 m_\phi^0 [\hat{O}M_0(r)] - j \frac{g \mu_0 M_s}{\omega} m_r^0 \right), \quad \mu_{33} = 1 + \alpha \frac{g^2 \mu_0^2 M_s^2}{\omega^2} ((m_r^0)^2 + (m_\theta^0)^2) [\hat{O}M_0(r)], \quad (A3)$$

$$\mu_{21} = \mu_{12}^*, \quad \mu_{31} = \mu_{13}^*, \quad \mu_{32} = \mu_{23}^* \quad (A4)$$

where

$$\alpha = \frac{1}{1 - \frac{g^2 \mu_0^2 M_s^2}{\omega^2} [\hat{O}M_0(r)]^2}, \quad \hat{O} = \left(\frac{\partial^2}{\partial r^2} + \frac{2}{r} \frac{\partial}{\partial r} - \frac{2}{r^2} \right) + 2\nu (1 - M_0^2) \quad (A5)$$

Here δ_{ij} is the Kronecker delta function, the asterisk denotes a complex conjugate and ω is an excitation angular frequency.

Appendix B: Block Matrices in Spherical Coupled-Wave Analysis

Expressions of the block matrices $\Psi_{qq'}$ in (9) are explicitly written as:

$$\Psi_{11} = 0, \quad \Psi_{12} = -\frac{1}{j\eta} [\mu_{13}^*] [\mu_{11}]^{-1} [j\pi p], \quad \Psi_{13} = -([\mu_{23}^*] - [\mu_{13}^*] [\mu_{11}]^{-1} [\mu_{12}]), \quad (B1)$$

$$\Psi_{14} = -\frac{1}{\eta^2} [\sqrt{1-\kappa^2}] [j\pi p] \left[\frac{1}{\epsilon_r} \right] [j\pi p] - \left[\frac{\mu_{33}}{\sqrt{1-\kappa^2}} \right] + [\mu_{13}^*] [\mu_{11}]^{-1} \left[\frac{\mu_{13}}{\sqrt{1-\kappa^2}} \right], \quad \Psi_{21} = 0, \quad (B2)$$

$$\Psi_{22} = \frac{1}{j\eta} \left[\frac{1}{\sqrt{1-\kappa^2}} \right]^{-1} [\mu_{12}^*] [\mu_{11}]^{-1} [j\pi p], \quad \Psi_{23} = \left[\frac{1}{\sqrt{1-\kappa^2}} \right]^{-1} ([\mu_{22}] - [\mu_{12}^*] [\mu_{11}]^{-1} [\mu_{12}]), \quad (B3)$$

$$\Psi_{24} = \left[\frac{1}{\sqrt{1-\kappa^2}} \right]^{-1} \cdot \left(\left[\frac{\mu_{23}}{\sqrt{1-\kappa^2}} \right] - [\mu_{12}^*] [\mu_{11}]^{-1} \left[\frac{\mu_{13}}{\sqrt{1-\kappa^2}} \right] \right), \quad \Psi_{31} = 0, \quad (B4)$$

$$\Psi_{32} = \left[\frac{\epsilon_r}{\sqrt{1-\kappa^2}} \right] + \frac{1}{\eta^2} \left[\sqrt{1-\kappa^2} \right] [j\pi p] [\mu_{11}]^{-1} [j\pi p], \quad (B5)$$

$$\Psi_{33} = \frac{1}{j\eta} \left[\sqrt{1-\kappa^2} \right] [j\pi p] [\mu_{11}]^{-1} [\mu_{12}], \quad \Psi_{34} = \frac{1}{j\eta} \left[\sqrt{1-\kappa^2} \right] [j\pi p] [\mu_{11}]^{-1} \left[\frac{\mu_{13}}{\sqrt{1-\kappa^2}} \right], \quad (B6)$$

$$\Psi_{41} = -[\epsilon_r] \left[\frac{1}{\sqrt{1-\kappa^2}} \right]^{-1}, \quad \Psi_{42} = 0, \quad \Psi_{43} = 0, \quad \Psi_{44} = 0, \quad (B7)$$

with

$$([\Upsilon])_{n,m} = \frac{1}{2} \int_{-1}^1 \Upsilon(\kappa) e^{-j(n-m)\pi\kappa} d\kappa \quad (B8)$$

Here, $[\Upsilon]$ is a square matrix generated by the Fourier coefficients of Υ , with (n, m) entries equal to Υ_{n-m} ; $\eta = k_0 r$.

Appendix C: Expansion of the Incident Field

The sources of the lowest-order spherical waves are current elements. As it is well-known a single electric-current (an elementary Hertz dipole) with current I and length l parallel to the z -axis radiates a TM_z field that can be derived from a magnetic vector potential. When the dipole is displaced off the origin, a radial wavefunction of the zero-th order is employed and for the radial component of the magnetic vector potential we have

$$A_r = r \frac{k_0 Il}{j4\pi h} h_0^{(2)}(k_0 |\mathbf{r} - \mathbf{h}|), \quad (C1)$$

where $\mathbf{h} = \mathbf{z}h$ and $h_0^{(2)}$ is the spherical Hankel function. Here h is a distance from the global origin to the source

location along the z -axis. Since (C1) is written in the coordinate system viewed from the source, we need to expand (C1) in spherical wavefunctions referred to the global origin. This can be accomplished using the addition theorem for the spherical functions, and finally we get

$$A_r = r \frac{k_0 Il}{j4\pi h} \sum_{n=0}^{\infty} (2n+1) h_n^{(2)}(k_0 r_>) j_n(k_0 r_<) P_n^0(\cos\theta) \quad (C2)$$

with $r_> = \max[r, h]$, $r_< = \min[r, h]$ and j_n is the spherical Bessel function of the n -th order. The electric and magnetic field components can be expressed through the radial component of the magnetic vector potential [89] and then can be directly implemented into our formalism (see Sec. III).

The analysis is straightforward for radially and azimuthally polarized beams. Assuming that the incident beam is propagating along the z -axis, we can expand the cylindrical wave functions in terms of spherical ones

[101]

$$J_m(k_\perp \rho) e^{jk_{||}z} = \sum_{n=0}^{\infty} j^n (2n+2m+1) \frac{n!}{(n+2m)!} \cdot \quad (C3)$$

$$P_{n+m}^m(\cos\theta) P_{n+m}^m(\cos\alpha) j_{n+m}(k_0 r).$$

Here k_\perp and $k_{||}$ are the wavenumbers along the transversal and longitudinal directions with respect to

propagation axis, i.e. z -axis, J_m is the Bessel function of the first kind with order n and α is an angle between the wavevectors \mathbf{k}_0 and \mathbf{k}_\perp . Finally, it is required to expand the θ -dependent terms in (C3) into a 1-D Fourier series as was done in (8) and impose the boundary conditions on the spherical shell surfaces to determine the unknown scattering coefficients. No modification of the formalism is needed.

[1] T. H. R. Skyrme, A non-linear field theory, Proceedings of the Royal Society of London. Series A. Mathematical and Physical Sciences **260**, 127 (1961).

[2] L. D. Faddeev, Some comments on the many-dimensional solitons, Letters in Mathematical Physics **1**, 289 (1976).

[3] E. Kuznetsov and A. Mikhailov, On the topological meaning of canonical Clebsch variables, Physics Letters A **77**, 37 (1980).

[4] E. Babaev, L. D. Faddeev, and A. J. Niemi, Hidden symmetry and knot solitons in a charged two-condensate Bose system, Phys. Rev. B **65**, 100512 (2002).

[5] M. M. Salomaa and G. E. Volovik, Vortices with ferromagnetic superfluid core in ${}^3\text{He-B}$, Phys. Rev. Lett. **51**, 2040 (1983).

[6] Bouligand, Y., Derrida, B., Poenaru, V., Pomeau, Y., and Toulouse, G., Distortions with double topological character: The case of cholesterics, J. Phys. France **39**, 863 (1978).

[7] A. Kosevich, B. Ivanov, and A. Kovalev, Magnetic solitons, Physics Reports **194**, 117 (1990).

[8] I. Bogolubsky, Three-dimensional topological solitons in the lattice model of a magnet with competing interactions, Physics Letters A **126**, 511 (1988).

[9] A. F. Rañada, A topological theory of the electromagnetic field, Letters in Mathematical Physics **18**, 97 (1989).

[10] A. Bogdanov and A. Hubert, Thermodynamically stable magnetic vortex states in magnetic crystals, Journal of Magnetism and Magnetic Materials **138**, 255 (1994).

[11] R. Rajaraman, Solitons and Instantons: An Introduction to Solitons and Instantons in Quantum Field Theory, Elsevier (1982).

[12] U. K. Rößler, A. N. Bogdanov, and C. Pfleiderer, Spontaneous skyrmion ground states in magnetic metals, Nature **442**, 797 (2006).

[13] S. Mühlbauer, B. Binz, F. Jonietz, C. Pfleiderer, A. Rosch, A. Neubauer, R. Georgii, and P. Böni, Skyrmion lattice in a chiral magnet, Science **323**, 915 (2009).

[14] X. Z. Yu, Y. Onose, N. Kanazawa, J. H. Park, J. H. Han, Y. Matsui, N. Nagaosa, and Y. Tokura, Real-space observation of a two-dimensional skyrmion crystal, Nature **465**, 901 (2010).

[15] S. Seki, X. Z. Yu, S. Ishiwata, and Y. Tokura, Observation of skyrmions in a multiferroic material, Science **336**, 198 (2012).

[16] N. Romming, C. Hanneken, M. Menzel, J. E. Bickel, B. Wolter, K. von Bergmann, A. Kubetzka, and R. Wiesendanger, Writing and deleting single magnetic skyrmions, Science **341**, 636 (2013).

[17] A. K. Yadav, C. T. Nelson, S. L. Hsu, Z. Hong, J. D. Clarkson, C. M. Schlepütz, A. R. Damodaran, P. Shafer, E. Arenholz, L. R. Dedon, D. Chen, A. Vishwanath, A. M. Minor, L. Q. Chen, J. F. Scott, L. W. Martin, and R. Ramesh, Observation of polar vortices in oxide superlattices, Nature **530**, 198 (2016).

[18] N. Kent, N. Reynolds, D. Raftrey, I. T. G. Campbell, S. Virasawmy, S. Dhuey, R. V. Chopdekar, A. Hierro-Rodriguez, A. Sorrentino, E. Pereiro, S. Ferreira, F. Hellman, P. Sutcliffe, and P. Fischer, Creation and observation of hopfions in magnetic multilayer systems, Nature Communications **12**, 1562 (2021).

[19] R. Wiesendanger, Nanoscale magnetic skyrmions in metallic films and multilayers: a new twist for spintronics, Nature Reviews Materials **1**, 16044 (2016).

[20] Y. Shen, Q. Zhang, P. Shi, L. Du, X. Yuan, and A. V. Zayats, Optical skyrmions and other topological quasi-particles of light, Nature Photonics **18**, 15 (2024).

[21] B. Dieny, I. L. Prejbeanu, K. Garello, P. Gambardella, P. Freitas, R. Lehndorff, W. Raberg, U. Ebels, S. O. Demokritov, J. Akerman, A. Deac, P. Pirro, C. Adelmann, A. Anane, A. V. Chumak, A. Hirohata, S. Manganin, S. O. Valenzuela, M. C. Onbaşlı, M. d'Aquino, G. Prenat, G. Finocchio, L. Lopez-Diaz, R. Chantrell, O. Chubykalo-Fesenko, and P. Bortolotti, Opportunities and challenges for spintronics in the microelectronics industry, Nature Electronics **3**, 446 (2020).

[22] E. Feldtkeller, Mikromagnetisch stetige und unstetige magnetisierungskonfigurationen, Zeitschrift für Angewandte Physik **19**, 530 (1965).

[23] W. Döring, Point singularities in micromagnetism, Journal of Applied Physics **39**, 1006 (1968).

[24] Y. P. Kabanov, L. Dedukh, and V. Nikitenko, Bloch points in an oscillating Bloch line, JETP Lett. **49** (1989).

[25] R. Hertel, Ultrafast domain wall dynamics in magnetic nanotubes and nanowires, Journal of Physics: Condensed Matter **28**, 483002 (2016).

[26] R. Hertel and C. M. Schneider, Exchange explosions: Magnetization dynamics during vortex-antivortex annihilation, Phys. Rev. Lett. **97**, 177202 (2006).

[27] A. Wartelle, B. Trapp, M. Staňo, C. Thirion, S. Bochmann, J. Bachmann, M. Foerster, L. Aballe, T. O. Menteş, A. Locatelli, A. Sala, L. Cagnon, J.-C. Toussaint, and O. Fruchart, Bloch-point-mediated topological transformations of magnetic domain walls in cylindrical nanowires, Phys. Rev. B **99**, 024433

(2019).

[28] A. Thiaville, J. M. García, R. Dittrich, J. Miltat, and T. Schrefl, Micromagnetic study of bloch-point-mediated vortex core reversal, *Phys. Rev. B* **67**, 094410 (2003).

[29] C. Blanco-Roldán, C. Quirós, A. Sorrentino, A. Hierro-Rodríguez, L. M. Álvarez-Prado, R. Valcárcel, M. Duch, N. Torras, J. Esteve, J. I. Martín, M. Vélez, J. M. Alameda, E. Pereiro, and S. Ferrer, Nanoscale imaging of buried topological defects with quantitative x-ray magnetic microscopy, *Nature Communications* **6**, 8196 (2015).

[30] N. Kanazawa, Y. Nii, X.-X. Zhang, A. S. Mishchenko, G. De Filippis, F. Kagawa, Y. Iwasa, N. Nagaosa, and Y. Tokura, Critical phenomena of emergent magnetic monopoles in a chiral magnet, *Nature Communications* **7**, 11622 (2016).

[31] M.-Y. Im, H.-S. Han, M.-S. Jung, Y.-S. Yu, S. Lee, S. Yoon, W. Chao, P. Fischer, J.-I. Hong, and K.-S. Lee, Dynamics of the bloch point in an asymmetric permalloy disk, *Nature Communications* **10**, 593 (2019).

[32] M. T. Birch, D. Cortés-Ortuño, K. Litzius, S. Wintz, F. Schulz, M. Weigand, A. Štefančič, D. A. Mayoh, G. Balakrishnan, P. D. Hatton, and G. Schütz, Toggle-like current-induced bloch point dynamics of 3d skyrmion strings in a room temperature nanowire, *Nature Communications* **13**, 3630 (2022).

[33] Y. Li, L. Pierobon, M. Charilaou, H.-B. Braun, N. R. Walet, J. F. Löfller, J. J. Miles, and C. Moutafis, Tunable terahertz oscillation arising from bloch-point dynamics in chiral magnets, *Phys. Rev. Res.* **2**, 033006 (2020).

[34] A. Rana, C.-T. Liao, E. Iacocca, J. Zou, M. Pham, X. Lu, E.-E. C. Subramanian, Y. H. Lo, S. A. Ryan, C. S. Bevis, R. M. Karl, A. J. Glaid, J. Rable, P. Mahale, J. Hirst, T. Ostler, W. Liu, C. M. O’Leary, Y.-S. Yu, K. Bustillo, H. Ohldag, D. A. Shapiro, S. Yazdi, T. E. Mallouk, S. J. Osher, H. C. Kapteyn, V. H. Crespi, J. V. Badding, Y. Tserkovnyak, M. M. Murnane, and J. Miao, Three-dimensional topological magnetic monopoles and their interactions in a ferromagnetic meta-lattice, *Nature Nanotechnology* **18**, 227 (2023).

[35] A. S. Koshikawa, J. Llandro, M. Ohzeki, S. Fukami, H. Ohno, and N. Leo, Magnetic order in nanoscale gyroid networks, *Phys. Rev. B* **108**, 024414 (2023).

[36] C. Zambrano-Rabanal, B. Valderrama, F. Tejo, R. G. Elías, A. S. Nunez, V. L. Carvalho-Santos, and N. Vidal-Silva, Magnetostatic interaction between bloch point nanospheres, *Scientific Reports* **13**, 7171 (2023).

[37] E. Saavedra, F. Tejo, N. Vidal-Silva, and J. Escrig, Symmetry breaking-induced resonance dynamics in bloch point nanospheres: Unveiling magnetic volume effects and geometric parameters for advanced applications in magnetic sensing and spintronics, *ACS Applied Materials & Interfaces* **16**, 27605 (2024).

[38] R. G. Elías, V. L. Carvalho-Santos, A. S. Núñez, and A. D. Verga, Spin waves scattering on a bloch point, *Phys. Rev. B* **90**, 224414 (2014).

[39] Topology and geometry of BP: Considering a closed surface enclosing the BP at its center, the direction of unit magnetization vector field (\mathbf{m}_0 in Eq.4) covers an integer number of times, a whole solid angle. Expressed in spherical coordinates [23], this vector field is parameterized by a polar component expressible as $p\theta$, and an azimuthal component written as $q\phi + \gamma$. Since \mathbf{m}_0 is single valued, q and p are integer number and the topological nature of the BP is then set by the quantity $Q = pq$, called the topological charge [11]. γ determines the geometry: It is an azimuthal tilt with regard to the radial direction, causing the BP to twist around z , as discussed in the text and shown in Fig.(3). Such as behavior and how the system goes from one q, p state to another is illustrated for example in [?] for vortices and skyrmions using micromagnetic simulations. The discussions and numerical calculations presented in this work assumes a specific γ . The actual value of γ for a given material depends on terms in the magneto-static energy, such as the dipolar energy [23], that are not in the focus of this work.

[40] Energy scale: In the region around the BP the dominant energy contribution stems from exchange energy $\int d^3\mathbf{r} \frac{J}{2a} (\nabla \mathbf{S})$, where J is the exchange interaction, a is the lattice constant and $\hbar S$ is the molecular spin which is proportional to the magnetization \mathbf{M} appearing in (2). The energy scale is typically an order of magnitude higher than that due to dipolar interactions which govern magneto-static excitations (spin waves) in uniform magnetic media.

[41] Q. Zhan, Cylindrical vector beams: from mathematical concepts to applications, *Adv. Opt. Photon.* **1**, 1 (2009).

[42] C. Rosales-Guzmán, B. Ndagano, and A. Forbes, A review of complex vector light fields and their applications, *Journal of Optics* **20**, 123001 (2018).

[43] R. Grunwald and M. Bock, Needle beams: a review, *Advances in Physics: X* **5**, 1736950 (2020).

[44] J. Wang and Y. Liang, Generation and detection of structured light: a review, *Frontiers in Physics* **9**, 688284 (2021).

[45] Z. H. Jiang and D. H. Werner, Electromagnetic vortices: wave phenomena and engineering applications, John Wiley & Sons (2021).

[46] Y. Kozawa, Y. Uesugi, and S. Sato, Characteristics of vector beam and its applications, *Photonics Review* **2025**, 250202 (2025).

[47] A. Vogliardi, G. Ruffato, D. Bonaldo, S. Dal Zilio, and F. Romanato, Azimuthally-variant perfect vector beams for the control of arbitrary phase and polarization ring patterns, *Light: Science & Applications* **14**, 183 (2025).

[48] M. Fanciulli, M. Pancaldi, A.-E. Stanciu, M. Guer, E. Pedersoli, D. De Angelis, P. c. v. Rebernik Ribič, D. Bresteau, M. Luttmann, P. Carrara, A. Ravindran, B. Rösner, C. David, C. Spezzani, M. Manfredda, R. Sousa, L. Vila, I. L. Prejbeanu, L. D. Budă-Prejbeanu, B. Dieny, G. De Ninno, F. Capotondi, T. Ruchon, and M. Sacchi, Magnetic vortex dynamics probed by time-resolved magnetic helicoidal dichroism, *Phys. Rev. Lett.* **134**, 156701 (2025).

[49] J. Wätzel, P. c. v. Rebernik Ribič, M. Coreno, M. B. Danailov, C. David, A. Demidovich, M. Di Fraia, L. Giannessi, K. Hansen, i. c. v. Krušič, M. Manfredda, M. Meyer, A. Mihelič, N. Mirian, O. Plekan, B. Ressel, B. Rösner, A. Simoncig, S. Spampinati, M. Stupar, M. c. v. Žitnik, M. Zangrandi, C. Callegari, J. Berak-

dar, and G. De Ninno, Light-induced magnetization at the nanoscale, *Phys. Rev. Lett.* **128**, 157205 (2022).

[50] J. R. Rouxel, B. Rösner, D. Karpov, C. Bacellar, G. F. Mancini, F. Zinna, D. Kinschel, O. Cannelli, M. Opfermann, C. Svetina, A. Diaz, J. Lacour, C. David, and M. Chergui, Hard x-ray helical dichroism of disordered molecular media, *Nature Photonics* **16**, 570 (2022).

[51] J. R. Rouxel and S. Mukamel, Molecular chirality and its monitoring by ultrafast x-ray pulses, *Chemical Reviews* **122**, 16802 (2022).

[52] T. Bose and J. Berakdar, Nonlinear magneto-optical response to light carrying orbital angular momentum, *Journal of Optics* **16**, 125201 (2014).

[53] G. De Ninno, J. Wätzel, P. R. Ribič, E. Allaria, M. Coreno, M. B. Danailov, C. David, A. Demidovich, M. Di Fraia, L. Giannessi, K. Hansen, Š. Krušič, M. Manfredda, M. Meyer, A. Mihelič, N. Mirian, O. Plekan, B. Ressel, B. Rösner, A. Simoncig, S. Spampinati, M. Stupar, M. Žitnik, M. Zangrandi, C. Callegari, and J. Berakdar, Photoelectric effect with a twist, *Nature Photonics* **14**, 554 (2020).

[54] S. Lin, Z. Nie, W. Yan, Y. Liang, H. Lin, Q. Zhao, and B. Jia, All-optical vectorial control of multistate magnetization through anisotropy-mediated spin-orbit coupling, *Nanophotonics* **8**, 2177 (2019).

[55] M. Fanciulli, D. Bresteau, M. Vimal, M. Luttmann, M. Sacchi, and T. Ruchon, Electromagnetic theory of helicoidal dichroism in reflection from magnetic structures, *Phys. Rev. A* **103**, 013501 (2021).

[56] M. Fanciulli, M. Pancaldi, E. Pedersoli, M. Vimal, D. Bresteau, M. Luttmann, D. De Angelis, P. c. v. R. Ribič, B. Rösner, C. David, C. Spezzani, M. Manfredda, R. Sousa, I.-L. Prejbeanu, L. Vila, B. Dieny, G. De Ninno, F. Capotondi, M. Sacchi, and T. Ruchon, Observation of magnetic helicoidal dichroism with extreme ultraviolet light vortices, *Phys. Rev. Lett.* **128**, 077401 (2022).

[57] L. Gao, S. Prokhorenko, Y. Nahas, and L. Bellaiche, Dynamical control of topology in polar skyrmions via twisted light, *Phys. Rev. Lett.* **132**, 026902 (2024).

[58] J. Wätzel and J. Berakdar, All-optical generation and ultrafast tuning of non-linear spin hall current, *Scientific Reports* **8**, 17102 (2018).

[59] J. Wätzel and J. Berakdar, Open-circuit ultrafast generation of nanoscopic toroidal moments: The swift phase generator, *Advanced Quantum Technologies* **2**, 1800096 (2019).

[60] G. F. Quinteiro Rosen, P. I. Tamborenea, and T. Kuhn, Interplay between optical vortices and condensed matter, *Rev. Mod. Phys.* **94**, 035003 (2022).

[61] T. Ozawa, H. M. Price, A. Amo, N. Goldman, M. Hafezi, L. Lu, M. C. Rechtsman, D. Schuster, J. Simon, O. Zilberberg, and I. Carusotto, Topological photonics, *Rev. Mod. Phys.* **91**, 015006 (2019).

[62] Z. Wang, Y. Chong, J. D. Joannopoulos, and M. Soljačić, Observation of unidirectional backscattering-immune topological electromagnetic states, *Nature* **461**, 772 (2009).

[63] M. Fanciulli, M. Pancaldi, A.-E. Stanciu, M. Guer, E. Pedersoli, D. De Angelis, P. Rebernik Ribič, D. Bresteau, M. Luttmann, P. Carrara, et al., Magnetic vortex dynamics probed by time-resolved magnetic helicoidal dichroism, *Physical Review Letters* **134**, 156701 (2025).

[64] M. Luttmann, M. Fanciulli, P. Carrara, M. Sacchi, and T. Ruchon, Optical spin-orbit interaction induced by magnetic textures, *arXiv preprint arXiv:2506.15232* (2025).

[65] R. Sultana, A. K. Mondal, V. S. Bhat, K. Stenning, Y. Li, D. M. Arroo, A. Vasdev, M. R. McCarter, L. E. De Long, J. T. Hastings, J. C. Gartside, and M. B. Jungfleisch, Ice sculpting: An artificial spin ice tutorial on controlling microstate and geometry for magnonics and neuromorphic computing, *Journal of Applied Physics* **138**, 061101 (2025).

[66] L. Berchialla, G. M. Macauley, and L. J. Heyderman, Focus on three-dimensional artificial spin ice, *Applied Physics Letters* **125**, 220501 (2024).

[67] M. Gołębiewski, R. Hertel, M. d'Aquino, V. Vasyuchka, M. Weiler, P. Pirro, M. Krawczyk, S. Fukami, H. Ohno, and J. Llandro, Collective spin-wave dynamics in gyroid ferromagnetic nanostructures, *ACS Applied Materials & Interfaces* **16**, 22177 (2024), pMID: 38648102, <https://doi.org/10.1021/acsami.4c02366>.

[68] N. Geerits, H. Lemmel, A.-S. Berger, and S. Sponar, Phase vortex lattices in neutron interferometry, *Communications Physics* **6**, 209 (2023).

[69] Q. Le Thien, S. McKay, R. Pynn, and G. Ortiz, Spin-textured neutron beams with orbital angular momentum, *Phys. Rev. B* **107**, 134403 (2023).

[70] M. E. Henderson, B. Heacock, M. Bleuel, D. G. Cory, C. Heikes, M. G. Huber, J. Krzywon, O. Nahman-Levesqué, G. M. Luke, M. Pula, D. Sarenac, K. Zhernenkov, and D. A. Pushin, Three-dimensional neutron far-field tomography of a bulk skyrmion lattice, *Nature Physics* **19**, 1617 (2023).

[71] D. Sarenac, M. E. Henderson, H. Ekinci, C. W. Clark, D. G. Cory, L. DeBeer-Schmitt, M. G. Huber, O. Lailey, J. S. White, K. Zhernenkov, and D. A. Pushin, Small-angle scattering interferometry with neutron orbital angular momentum states, *Nature Communications* **15**, 10785 (2024).

[72] V. Jandieri, R. Khomeriki, L. Chotorlishvili, K. Watanabe, D. Erni, D. H. Werner, and J. Berakdar, Photonic signatures of spin-driven ferroelectricity in multiferroic dielectric oxides, *Phys. Rev. Lett.* **127**, 127601 (2021).

[73] R. G. Elías and A. Verga, Magnetization structure of a bloch point singularity, *The European Physical Journal B* **82**, 159 (2011).

[74] Directly at the BP where the magnetization vanishes (cf. Fig.1) atomistic models are needed. The theory presented here does not include this particular point. A reasonable length beyond which our model is expected to hold is set by the exchange length $\sqrt{J/(M_s^2 a)}$, the value of this length is ≈ 6 nm for Permalloy. Since our focus is not on describing BPs as such but on the behavior of the EM fields scattering from BPs, and the fields do not scatter when $M_s = 0$, this issue is less critical for this study.

[75] M. Lang, M. Beg, O. Hovorka, and H. Fangohr, Bloch points in nanostrips, *Scientific Reports* **13**, 6910 (2023).

[76] Our formulation based on Eqs.(1, 2) captures the physics of BPs. It does not include the magnetic material well beyond BP. This part enters our the-

ory/simulations through a finite but constant relative permeability. Field matching is performed between the BP region and the surrounding rendering the EM fields well-defined in the whole space. Note, typically the response of the exchange-dominated BP is at a different (higher) frequency than the magneto-statically-coupled region with a response in the GHz. Mathematically this means that within our formulation and boundary conditions, we cannot realize BP as localized solutions in a vector field which is spatially homogeneous, meaning collinear at infinity.

[77] D. Schulz, B. Schwager, and J. Berakdar, Nanostructured spintronic emitters for polarization-textured and chiral broadband THz fields, *ACS Photonics* **9**, 1248 (2022).

[78] J. M. Jarem, Rigorous coupled-wave-theory analysis of dipole scattering from a three-dimensional, inhomogeneous, spherical dielectric, and permeable system, *IEEE transactions on microwave theory and techniques* **45**, 1193 (2002).

[79] J. Jarem, Rigorous coupled wave theory solution of phi-periodic circular cylindrical dielectric systems, *Journal of Electromagnetic Waves and Applications* **11**, 197 (1997).

[80] V. Jandieri, R. Khomeriki, L. Chotorlishvili, K. Watanabe, D. Erni, D. H. Werner, and J. Berakdar, Photonic signatures of spin-driven ferroelectricity in multiferroic dielectric oxides, *Phys. Rev. Lett.* **127**, 127601 (2021).

[81] I. Moreno, J. A. Davis, I. Ruiz, and D. M. Cottrell, Decomposition of radially and azimuthally polarized beams using a circular-polarization and vortex-sensing diffraction grating, *Optics Express* **18**, 7173 (2010).

[82] Y. Shen, H. Wang, and S. Fan, Free-space topological optical textures: tutorial, *Advances in Optics and Photonics* **17**, 295 (2025).

[83] J. Chen, A. Forbes, and C.-W. Qiu, More than just a name? from magnetic to optical skyrmions and the topology of light, *Light: Science & Applications* **14**, 28 (2025).

[84] A. A. Wang, Z. Zhao, Y. Ma, Y. Cai, R. Zhang, X. Shang, Y. Zhang, J. Qin, Z.-K. Pong, T. Marozsák, et al., Topological protection of optical skyrmions through complex media, *Light: Science & Applications* **13**, 314 (2024).

[85] V. Jandieri, R. Khomeriki, K. Watanabe, D. Erni, D. H. Werner, and J. Berakdar, Tunable chiral photonic cavity based on multiferroic layers, *Opt. Express* **31**, 26591 (2023).

[86] V. Jandieri, P. Baccarelli, G. Valerio, and G. Schettini, 1-d periodic lattice sums for complex and leaky waves in 2-d structures using higher order Ewald formulation, *IEEE Transactions on Antennas and Propagation* **67**, 2364 (2019).

[87] V. Jandieri and K. Yasumoto, Scattering and guidance by layered cylindrically periodic arrays of circular cylinders (Ch. 21 in book: "Advances in Mathematical Methods for Electromagnetics," Institution of Engineering and Technology (IET), 2020).

[88] R. Khomeriki, V. Jandieri, K. Watanabe, D. Erni, D. H. Werner, M. Alexe, and J. Berakdar, Photonic ferroelectric vortex lattice, *Physical Review B* **109**, 045428 (2024).

[89] R. F. Harrington, *Time-Harmonic Electromagnetic Fields* (2001).

[90] V. Jandieri, R. Khomeriki, K. Watanabe, D. Erni, D. H. Werner, and J. Berakdar, Chiral optical solitons in an electrically active multiferroic guiding structure, *Optics Express* **32**, 4327 (2024).

[91] K. Y. Bliokh, Y. S. Kivshar, and F. Nori, Magneto-electric effects in local light-matter interactions, *Phys. Rev. Lett.* **113**, 033601 (2014).

[92] Y. Tang and A. E. Cohen, Optical chirality and its interaction with matter, *Phys. Rev. Lett.* **104**, 163901 (2010).

[93] R. Li, J. Wang, X.-L. Qi, and S.-C. Zhang, Dynamical axion field in topological magnetic insulators, *Nature Physics* **6**, 284 (2010).

[94] L. Wu, M. Salehi, N. Koirala, J. Moon, S. Oh, and N. P. Armitage, Quantized Faraday and Kerr rotation and axion electrodynamics of a 3d topological insulator, *Science* **354**, 1124 (2016).

[95] D. M. Nenno, C. A. C. Garcia, J. Gooth, C. Felser, and P. Narang, Axion physics in condensed-matter systems, *Nature Reviews Physics* **2**, 682 (2020).

[96] S. Ghosh and C. Timm, Charge-spin response and collective excitations in Weyl semimetals, *Phys. Rev. B* **99**, 075104 (2019).

[97] A. Ghosh, S. Yang, Y. Dai, W. V. Liu, and H. Petek, Plasmonic vortices host magnetoelectric interactions, *Phys. Rev. Res.* **6**, 013163 (2024).

[98] K. Y. Bliokh, M. A. Alonso, E. A. Ostrovskaya, and A. Aiello, Angular momenta and spin-orbit interaction of nonparaxial light in free space, *Phys. Rev. A* **82**, 063825 (2010).

[99] J. Mun, M. Kim, Y. Yang, T. Badloe, J. Ni, Y. Chen, C.-W. Qiu, and J. Rho, Electromagnetic chirality: from fundamentals to nontraditional chiroptical phenomena, *Light: Science & Applications* **9**, 139 (2020).

[100] I. A. Yastremsky, Magnetization length in the bloch point at finite temperatures, *Journal of Magnetism and Magnetic Materials* **616**, 172834 (2025).

[101] J. A. Stratton, *Electromagnetic theory*, John Wiley & Sons (2007).